Data-driven shape sensing of a hypersonic inlet ramp

Luke Pollock
L.Pollock@adfa.edu.au
UNSW Canberra
School of Engineering and Technology
Campbell
Australia

Graham Wild
UNSW Canberra
School of Science
Campbell
Australia

ABSTRACT

This paper introduces shape sensing using fibre Bragg gratings (FBGs) for hypersonic applications. Accurate shape sensing for geometry sensitive surfaces such as inlet ramps and control surfaces is crucial for monitoring and maintaining vehicle performance, stability, and integrity. Firstly, a simple cantilever plate is examined from which the shape is reconstructed using both analytical and data driven approaches. Following this, surrogate data is generated from a finite element model of a scramjet inlet ramp to train several neural networks. The results show disparity between measured and predicted strains, likely as the result of errors in the model or in the bonding of the FBGs to the ramp. Strain correction factors are obtained from static load testing which improves the predictive capabilities of the network under static loads but reduces accuracy under dynamic loading, indicating the need for an autoregressive component.

Keywords: Hypersonic, scramjet, shape sensing, data-driven, fibre Bragg grating

NOMENCLATURE

HSV	Hypersonic vehicle
FTSI	Fluid-thermal-structural interaction
iFEM	Inverse finite element method
FOSS	Fibre optic sensing system
OFDR	Optical frequency domain reflectometry
FBG	Fibre Bragg grating
WLSF	Weighted least-squares function
FFNN	Feedforward neural network
CFNN	Cascadeforward neural network
RMSE	Root mean square error
SPS	Samples per second
PSD	Power spectral density
LM	Levenberg-Marquardt
BR	Bayesian regularisation
SCG	Scaled conjugate gradient

Symbols

Φ	Weighted least-squares function
$\boldsymbol{u}$	Kinematic variables
$\boldsymbol{e}$	Finite element section strain functions
$\boldsymbol{e}^{\epsilon}$	Experimental strain measurements
λ_B	Bragg wavelength
n	Refractive index
Λ	Grating period
Δ	Change in parameter
k_ϵ	Elastic coefficient
ϵ	Strain
k_T	Thermal coefficient
T	Temperature
p_{11}, p_{12}	Pockel's coefficients
α	Coefficient of thermal expansion
ξ	Thermo-optic coefficient
δ	Deflection
x	Distance along path
θ	Slope
ρ	Radius of curvature
κ	Curvature
t	Thickness
F	Force
E	Elastic (Young's) modulus
I	Moment of inertia
L	Length

1.0 INTRODUCTION

1.1 Hypersonic Flight

Hypersonic flight is typically defined as that which exceeds five times the freestream speed of sound (Mach 5). The extreme environments in which hypersonic vehicles (HSVs) operate have limited their proliferation, despite greater investment in recent years [1]. Airbreathing engines that employ compression ramps, such as ramjets and scramjets, are capable of generating the required thrust to maintain cruise at hypersonic speeds. These engines suffer from a limited window in which they can operate, requiring creative solutions such as morphing geometries, to extend their operating envelope. The Lockheed SR-71 Blackbird notably employed a retractable spike inlet, allowing it to operate efficiently from Mach 1.6 to 3.2. Another design challenge for hypersonic airbreathing engines is that of fluid-thermal-structural interaction (FTSI) [2, 3]. The high thermal and pressure loads can deform the compression ramp, reducing efficiency or in the extreme case, causing unstart, resulting in a loss of thrust and adverse moments that destabilise the vehicle [4, 5]. Unstart resulted in the loss of an SR-71 in 1966, and the death of the onboard flight test specialist, Jim Zwayer. 1

1.2 Shape Sensing

One area of interest that optical fibre sensors can excel, is that of shape sensing. The ability to provide quasi-real-time estimations of the shape of a vehicle that has inherent geometry dependent performance, allows for the evaluation of the state of its performance. Shape sensing may also be used as a means of providing data for design validation, health monitoring [6, 7], and in more exotic applications, as part of a shape morphing feedback loop [8]. A number of shape sensing algorithms have been proposed, including analytical methods such as Ko's displacement theory [9], data-driven approaches [10], and inverse finite element methods (iFEM) [11].

Whilst Ko's displacement theory derives itself from the mechanics of Euler-Bernoulli beams, it has been extended for the analysis of shear and torsion [12], as well as anisotropic materials [13]. The two-strain line method is a simple extension of the original theory to calculate the twist of a beam [14]. NASA Armstrong's fibre optic sensing system (FOSS), based on the optical frequency domain reflectometry (OFDR) method, which can interrogate thousands of FBGs, has been used in conjunction with Ko's displacement theory for the shape sensing of the MQ-9 Ikhana aircraft [14]. The sensing system is limited to a sampling frequency of 100 Hz, but has excellent spatial resolution and is hence, aptly suitable for the quasi-static shape sensing of aerospace structures [15].

Data driven shape sensing has interestingly been dominated by the robotics industry for pose and state estimation on primarily soft devices [16, 17]. The accuracy of the data driven approach is driven by the quality of the training data supplied, with the model itself capable of reconstructing non-linear deformations [17]. Manavi Roodsari, et al. [18] used a "Siamese network architecture" along with eccentric FBGs for the shape sensing of a minimally invasive surgical robot. The authors proposed that including time-dependent shape information in future versions would further improve the accuracy.

The inverse finite element method is a popular and powerful method for the shape sensing of complex structures. This approach relies on the minimisation of a weighted least-squares functional (WLSF) that is constructed from the finite element model, such as the one shown in Equation 1 [19].

$$\Phi(\boldsymbol{u}) = \|\boldsymbol{e}(\boldsymbol{u}) - \boldsymbol{e}^{\epsilon}\|^2 \tag{1}$$

Where $\boldsymbol{e}(\boldsymbol{u})$, are the section strains from the constructed finite element model and $\boldsymbol{e}^{\epsilon}$ are the measured experimental strains. A system of equation is produced that may be efficiently solved through a single matrix inversion. It is worth noting that unlike a typical finite element model, the iFEM approach does not require knowledge of the material properties or external loads to minimise the WLSF [20]. iFEM has been employed for the shape sensing of aerospace structures, including in conjunction with the NASA FOSS system for the detection of structural anomalies [21, 22].

Emerging hybrid methods such as the one developed by Pak [23] uses a two-step approach along with NASA FOSS. The first step employs Ko's displacement theory along a strain line, following which the calculated slopes and displacements are used as inputs to a finite element model. This hybrid method reconstructs the full-field displacement of a cantilever wing with less than 5% error in all assessed cases.

1.3 Fibre Bragg Gratings

The demands of hypersonic flight have led the development of low cost, small, sensitive, versatile, and durable sensors. Optical instrumentation provides many of these advantages, particularly over their conventional electrical counterparts. Fibre Bragg gratings (FBGs) are one such suitable technology. FBGs can be multiplexed, allowing for quasi-distributed sensing, and can easily be manufactured to sense a variety of measurands – including strain [24], temperature [25], corrosion [26], pH [25] and electromagnetics [27]. Such sensors can be manufactured by inscribing a photosensitive optical fibre with an ultraviolet laser, thereby creating a periodic refractive index in the core of the fibre. This inscription forms a wavelength specific mirror with a centre wavelength described by the Bragg wavelength as follows [24].

$$\lambda_B = 2n\Lambda \tag{2}$$

Where n is the effective refractive index and Λ is the grating period. The response of the FBG is derived from the theory of photoelasticity where the relative change in the Bragg wavelength is driven by the mechanical strains and temperature changes [28].

$$\frac{\Delta\lambda_B}{\lambda_B} = k_\epsilon \epsilon + k_T \Delta T \tag{3.1}$$

$$k_\epsilon = 1 - \frac{1}{2}n^2[p_{12} - \nu(p_{12} + p_{11})] \tag{3.2}$$

$$k_T = \left[1 - \frac{1}{2}n^2(p_{11} + 2p_{12})\right]\alpha + \frac{\xi}{n} \tag{3.3}$$

ϵ is the mechanical strain, ΔT is the change in temperature, ν is the fibre Poisson's ratio, p_{11} and p_{12} are Pocknel's coefficients, α is the fibre coefficient of thermal expansion, and ξ is the fibre thermo-optic coefficient. The dual-sensitivity of an FBG is often a challenge but can be valuable in cases – such as hypersonic flight – where the shape of a structure is affected by both the mechanical and thermal loading. Overall, FBGs offer many benefits over electrical instrumentation for both hypersonic flight, and the shape sensing of aerospace structures.

1.4 Summary

Despite the sensitivity of hypersonic vehicles to their shape, little-to-no work has been undertaken towards the development of shape sensing technologies for hypersonic vehicles. Hence, this paper aims to introduce the use of shape sensing for an applied hypersonic geometry to promote the field within the hypersonic community. First, a simple cantilever plate model is analysed using both analytical and data-driven approaches. Following this, a data driven model for a scramjet inlet ramp is developed using surrogate data generated from a finite element model of the structure. The effectiveness of the model is then compared against experimental data.

2.0 CANTILEVER MODEL

2.1 Setup

To first assess the efficacy of the neural network, a canonical case is selected from which analytical solutions are known. A finite element model of a simple aluminium cantilevered plate of 1 mm thickness and dimensions of (100 x 50)-mm is create. The plate is fixed on one end and a prescribed displacement applied to the other. Several methods are compared to reconstruct the midline out-of-plane displacement, including, data-driven, Ko's, and Euler-Bernoulli analytical. A feedforward and cascade forward neural network (FFNN and CFNN, respectively), are trained onto transient surrogate data by applying an impulse load to the free edge of the plate and measuring the strain at a

single location. The layouts of the two networks are shown in Figure 1. Ko's displacement theory and the Euler-Bernoulli analytical methods are discussed in the following section.

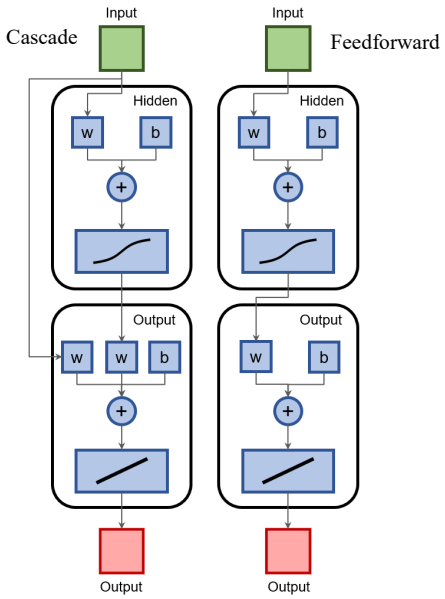

Figure 1 The network architecture of the cascade and feedforward neural networks.

2.2 Results and Discussion

The out-of-plane displacement and in-line strain along the midline of the cantilevered plate are shown in Figure 2. As evident, a 3 mm vertical deflection has been applied to the free edge of the plate.

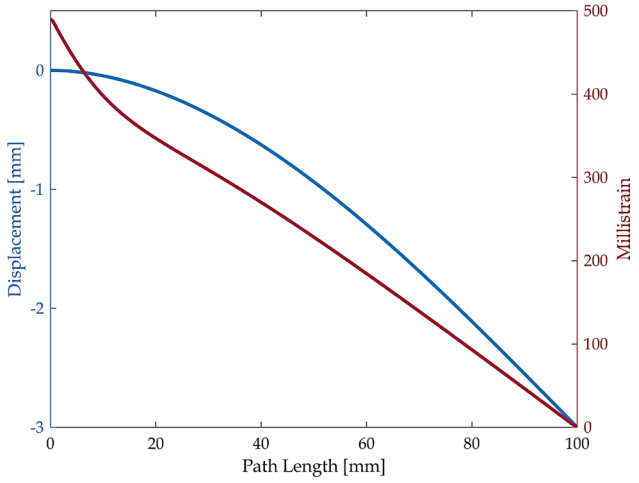

Figure 2 Displacement and strain along the midline of the cantilevered plate.

Firstly, we may derive a general expression for the out-of-plane displacement of a beam using Ko's displacement theory. Assuming the slope of the beam is approximately equal to the angle made between the horizontal and neutral axes, one obtains,

$$\frac{d\delta}{dx} = \theta_x \tag{4}$$

Following which, an infinitesimal length may be related to the curvature of the beam,

$$dx = \rho \, d\theta \tag{4.1}$$

$$\therefore \quad \frac{d\theta}{dx} = \frac{d^2\delta}{dx^2} = \frac{1}{\rho} = \kappa \tag{4.2}$$

Finally, expressing strain as $\frac{-t}{2}\kappa$, one obtains

$$\frac{d^2\delta}{dx^2} = \frac{-2}{t}\,\epsilon_x \tag{5}$$

Knowing the strain at one location on the panel along with the assumption of zero strain at the free end, either a constant strain or linear strain model may be used. A constant strain model (0^{th} order) results in a quadratic shape function, whilst a linear model (1^{st} order) produces a cubic shape function.

$$\delta_x = -\frac{1}{t}\epsilon_0 x^2, \quad O(1) \tag{6.1}$$

$$\delta_x = \frac{1}{3}\Psi x^3 - \left(\Psi x_0 + \frac{\epsilon_0}{t}\right)x^2, \qquad \Psi \equiv \frac{\epsilon_0}{t(L - x_0)}, \qquad O(n) \tag{6.2}$$

Using the strain data from the numerical model, the optimal location of the single strain sensor may then be determined. The root-mean-square error (RMSE) of the reconstructed shape and original shape is used as a measure of accuracy. Figure 3 shows the RMSE as a function of sensor location along the midline of the plate. For the 0^{th} order model, one minima is found whilst the 1^{st} order model shows three possible sensor locations. By evaluating the gradient of the RMSE, the sensor location may be down selected. The optimal location will have the smallest gradient to limit errors in sensor placement.

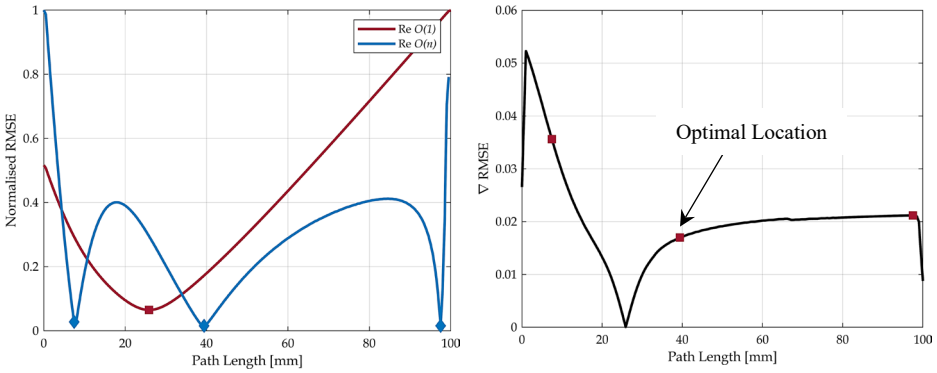

Figure 3 Plots of a) the normalised RMSE and b) the gradient of the RMSE along the midline path of the plate.

The final analytical method considered is that of a classical Euler-Bernoulli beam with an applied end load. This method is not applicable under normal circumstances because it relies upon knowledge that cannot be obtained from a strain sensor but provides a good baseline for comparison.

$$\delta_x = -\frac{F}{6EI}x^2(3L - x) \tag{7}$$

Results comparing the true deflection of the plate, along with the assessed reconstruction methods are shown in Figure 4. It is apparent that both data-driven methods overpredict the displacement of the plate but are capable of capturing the shape. Conversely, the 0^{th} order method cannot capture the shape of the plate but does a more reasonable job at estimated the magnitude of the displacement. Both the 1^{st} order and analytical solutions can reconstruct the true shape of the plate with negligible error.

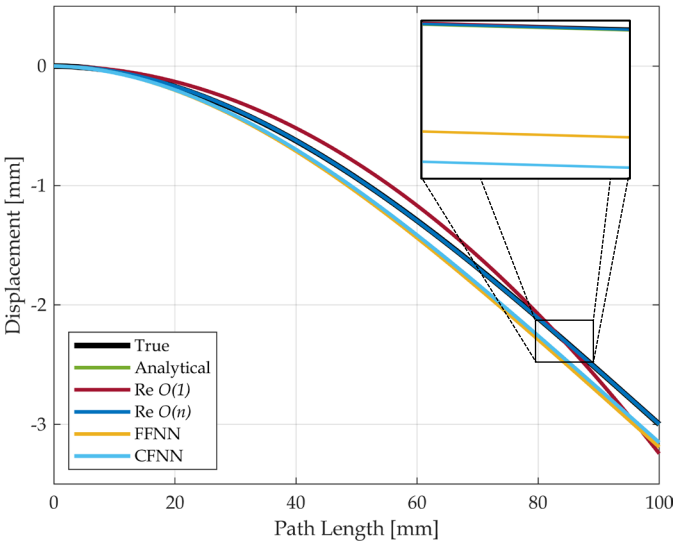

Figure 4 A comparison of techniques for the shape sensing of the cantilevered plate.

A comparison in error between all methods is shown in Figure 5. The RMSE reflects what can be observed in Figure 4. Despite the greatest errors being present in the data driven approaches, the RMSE remains less than 5% of the free edge deflection. As has been previously discussed, the accuracy of the data driven approaches is largely dependent upon the quality of the training data supplied. Nonetheless, all assessed methods prove potentially suitable.

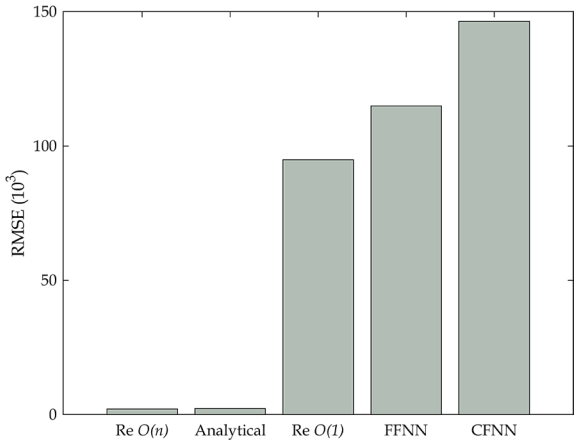

Figure 5 A comparison of the RMSE for each of the methods assessed.

3.0 INLET MODEL

3.1 Setup

The applied geometry assessed in this work is the inlet-ramp described by Bhattrai, et al. [29]. This geometry is a two-dimensional, three-shock mixed compression ramp designed to operate at Mach 5.85. The ramp surface is manufactured from nominally 3 mm aluminium with a body panel adhered to the leading edge composed of 0.3 mm bronze. A sketch of the ramp assembly is shown in Figure 6.

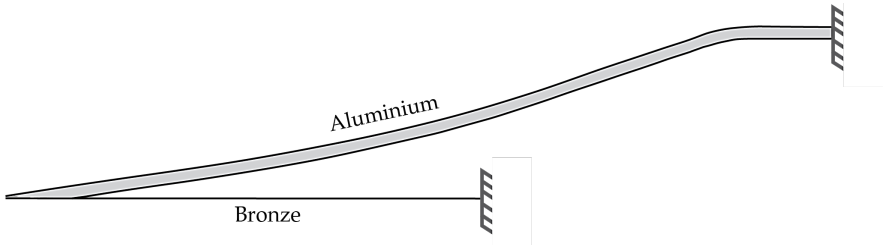

Figure 6 The configuration of the simply supported ramp with body panel.

Experimentally, a six-sensor layout using one line of multiplexed FBGs was bonded to the top surface of the ramp with the layout shown in Figure 7. Each grating is 10 mm long with a 50 mm spacing between them (end to end). The layout is symmetric around the midline of the panel. The FBGs are interrogated using a FS22 BraggMeter at 1,000 samples per second (SPS). Laser triangulation using a scanCONTROL 2750 provided two-dimensional profiles of the ramp at the same frequency.

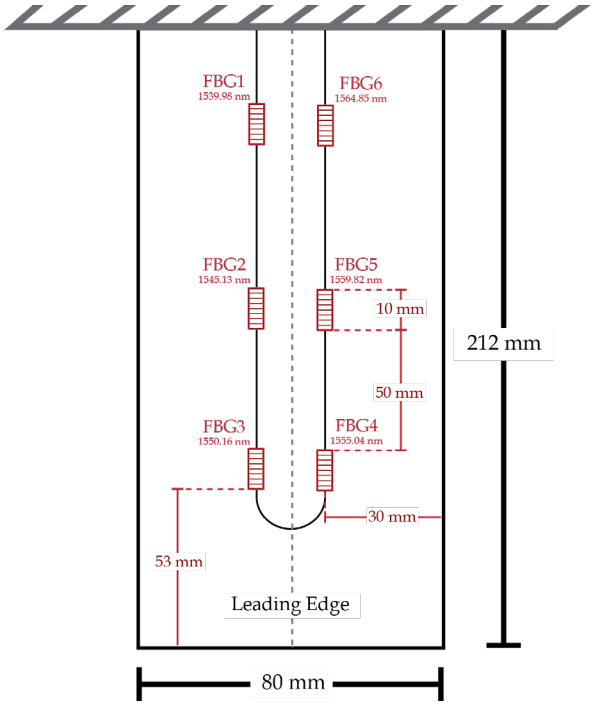

Figure 7 The FBG sensor layout on the compression ramp.

Firstly, static loading was conducted by hanging weights from both the centre of the leading edge and 20 mm offset – thereby generating a twist. This data was used to verify a finite element model of the ramp. Mechanical properties of both materials are given in Table 1.

Table 1
Mechanical properties of the materials that compose the ramp.

	Young's Modulus (GPa)	**Poisson's Ratio**	**Density (kg/m^3)**
Aluminium	71	0.33	2,770
Bronze	70	0.34	8,000

3.2 Numerical Model Validation

To generate the surrogate data, a numerical finite element model was constructed, which is shown in Figure 8.

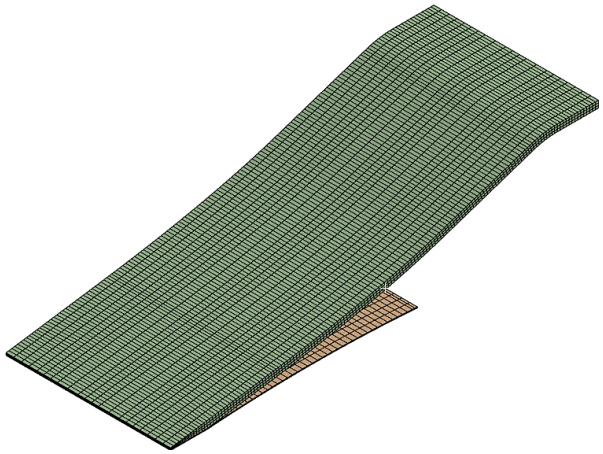

Figure 8 The mesh used for the numerical model.

3.2.1 Profile

To ensure that physical model matched the geometry of the digital part, the ramp was scanned using a laser profilometer. The profilometer could not measure the entire ramp, so only one profile was reconstructed from the leading edge as shown in Figure 9. The physical ramp profile matched very well with the digital model. The largest surface deviation observed in the single profile was 1.29 mm, equal to 0.3% of the total ramp height and 43% of the ramp thickness. This deviation is unlikely to have a large effect on the data produced, however, full scans of any geometry should be completed to either validate the physical model or to replace the original digital model.

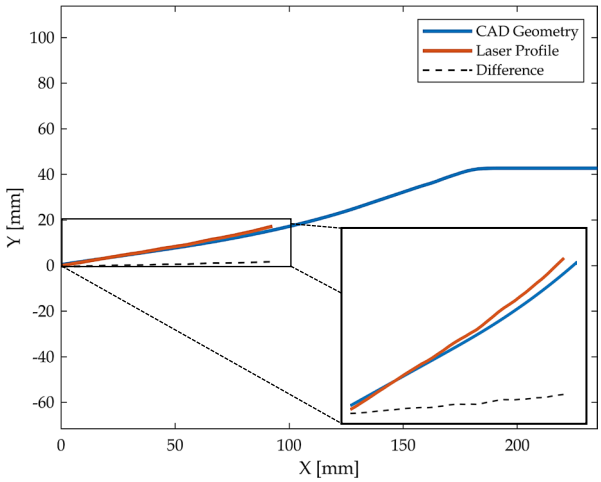

Figure 9 A comparison between the digital geometry and the shape attained from the laser scanner.

3.2.2 Modal Response

Next, we consider the modal response of the ramp to an impulse. Experimental data was obtained using a Polytech PDV-100 – a laser doppler vibrometer with a sampling frequency of 22 kHz. The spectral response of the model, normalised and plotted on a semi-log scale is shown in Figure 10. The first mode of the numerical model is plotted as the vertical dashed line. This matches well with the peak power spectral density.

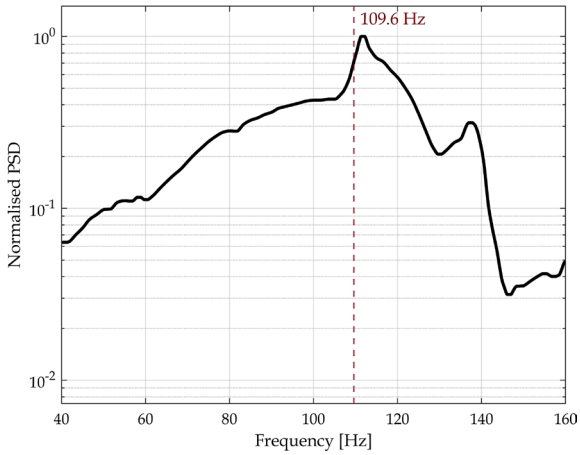

Figure 10 Normalised power spectral density (PSD) of the acquired laser vibrometer signal. First mode frequency of the numerical model is plotted as the dashed vertical red line.

3.2.3 Static Loading

Finally, we consider the static response of the ramp to an applied load. A first test is conducted by applying loads at the centre of the leading edge to measure pure bending, whilst a second test, applying loads 20 mm from the centre to induce twist is also conducted. A comparison between the experimental and finite element model are shown in Figure 11, with the two matching well. The model demonstrates a non-linear response to the applied load, likely as a result of the attached body panel. A maximum displacement of approximately 3.5 mm was assessed, a similar order to that observed in the original FSI experiments by Bhattrai, et al. [5].

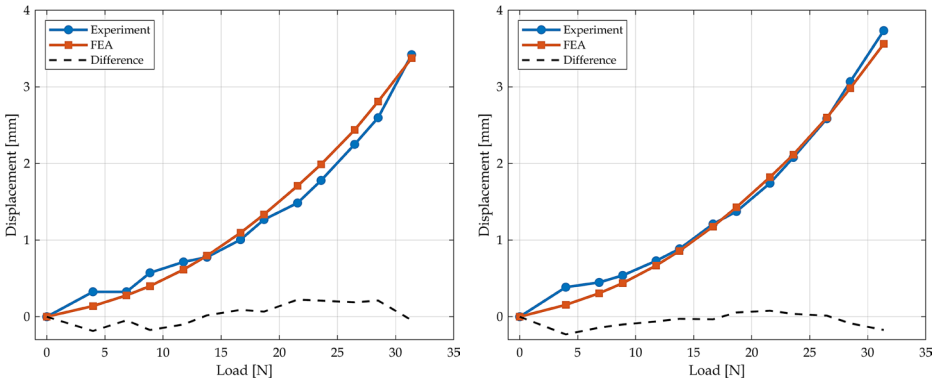

Figure 11 Validation of the numerical model for a) the centre load case and b) the offset load case.

3.2.4 FBG Correction Factors

Having deemed that the finite element model suitably matches the mechanical behaviour of the ramp, it is then possible to examine the accuracy between the expected strain and measured strain from the FBG sensors. Figure 12 provides a comparison between the experimental measurements on either side of the ramp under pure bending. FBG pairs respond almost identically, indicating symmetric in the measurement. However, there is a noticeable difference in the magnitude of the expected strains and in some cases, the trend. This could be the result of differences in the finite element model that have not been observed in the previous validation tests or from poor bonding of the FBGs. A crude attempt has been made to correct for the observable errors with a future investigation planned.

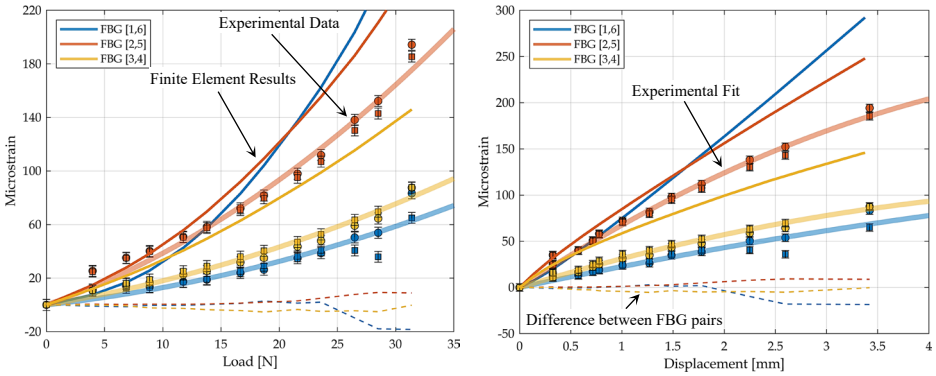

Figure 12 A comparison between the experimental and numerical strains obtained under the static testing.

Correction factors are obtained by taking the median ratio of the finite element results and experimental fits. The corrected experimental results more closely, but not perfectly, resemble the finite element results, as shown in Figure 13. Every effort should be taken to ensure FBGs can be accurately replicated by the numerical model. In this instance, it is likely there is poor bonding between the FBG and substrate, as well as some error in position, and orientation, that have contributed to the disagreement between results. Overall, it is observed that FBG pairs one through three, from root to leading edge, have measured 30.6%, 81.2%, and 54.9% of the predicted strain, respectively.

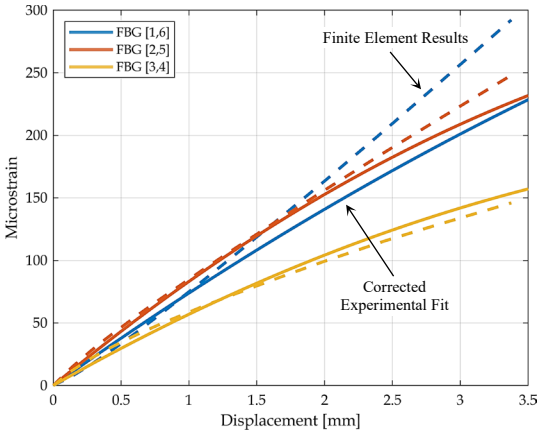

Figure 13 A plot of the corrected FBG strains in comparison to the original finite element results.

3.3 Generating Training Data

Ten equidistant control points were created on either side of the ramp from which vertical and horizontal displacements were measured in the global axis. Surrogate data was generated from the numerical model by applying an impulse load at each of the control points, either in pairs – to create bending, or individually – to create torsion. Strain measurements were taken in the local element frame as the average value over the 10 mm grating length using the layout pattern shown in Figure 7. A total of 168,000 input values were generated from the six simulated FBG sensors and 1,120,000 target values from the 20 control points (40 degrees-of-freedom).

3.4 Validating Training Data

Training data was randomly divided into three groups allotting, 70%, 15%, and 15% for the training, testing, and validation groups, respectively. A series of FFNNs and CFNNs were then trained and assessed using the Levenberg-Marquardt (LM), Bayesian regularisation (BR), and scaled conjugate gradient (SCG) training functions, the results of which are shown in Table 2.

Table 2
Results of the training on all six neural networks.

	Feedforward		Cascade Forward	
	Training time (s)	**RMSE (10^3)**	**Training time (s)**	**RMSE (10^3)**
LM	2,874	3.853	6,651	3.490
BR	5,986*	3.641	4,391	3.514
SCG	86	6.847	76	7.360

* Stopped after 1,000 epochs.

Both the LM and BR training functions performed similarly, whilst the SCG function trained the model rapidly but with larger errors. The SCG function also required less memory and hence, is more suitable for exceptionally large datasets. A comparison is also given in Figure 14, showing the RMSE of the out-of-plane displacements between the training data and model's prediction of the training data. The RMSE steadily decreases from leading edge to root, as would be expected, with a decrease in deflection magnitude.

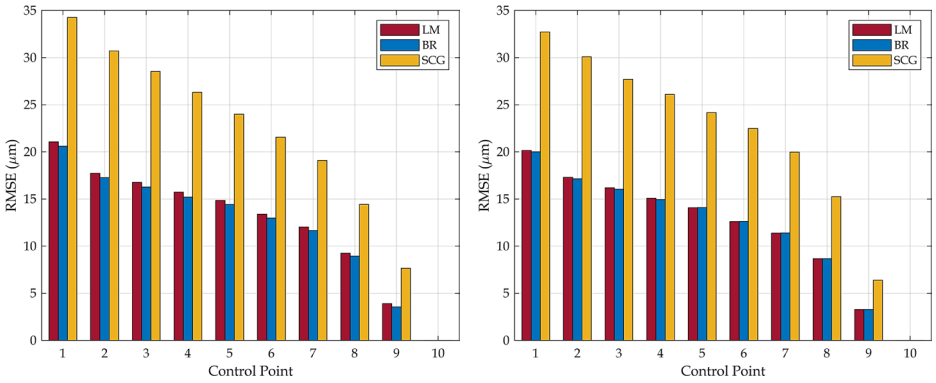

Figure 14 A comparison of RMSE of the out-of-plane displacement for the down-selected neural network at each of the control points.

Following this test, the six models were down selected to the cascade forward network trained using the Levenberg-Marquardt function. A histogram and corresponding normal probability density function of this model's error is shown in Figure 15. Results show no bias. Data outside of the 95% confidence interval is shaded grey.

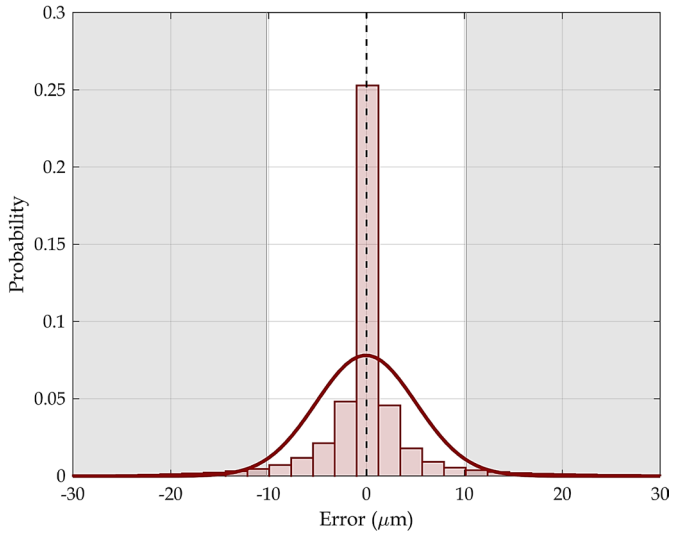

Figure 15 The error histogram of the down-selected neural network.

3.5 Static Testing

Next, the performance of the model was evaluated using the data for the static load testing. Figure 16 shows a comparison between the data obtained from the finite element model and that of the FBGs, both uncorrected and corrected. As expected, the uncorrected FBG

data underpredicts the displacement of the model. The corrected data does a reasonable job of predicting the static displacements but tends to underpredict the magnitude.

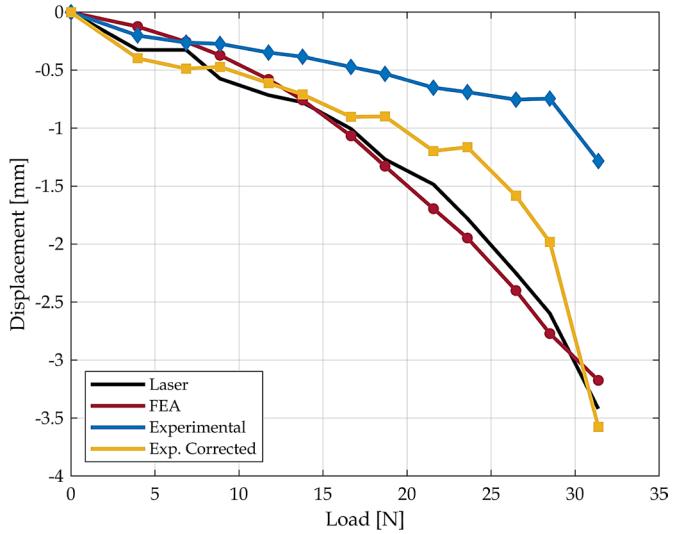

Figure 16 A comparison of the leading-edge ramp displacement obtained from the down-selected neural network using different datasets.

3.6 Dynamic Testing

The final test is conducted using the model to recreate the displacement of the ramp under the influence of random impulse loading. The out-of-plane displacement at the leading edge is plotted in Figure 17. Interestingly, under dynamic loading, the model tends to overpredict the magnitude of the deflection, even more so when using correction factors. This could imply that there is a transient phenomenon that is not being captured by the simple forward passing neural networks. There is also some observed signal inversion when applying the correction factors, likely as the result of an attempt to correct the difference in trends between the numerical and physical results. Hence, the simple correction method may not be suitable or should be applied with significant caution. Nonetheless, both the uncorrected and corrected results do well to capture the spectral information in the signal.

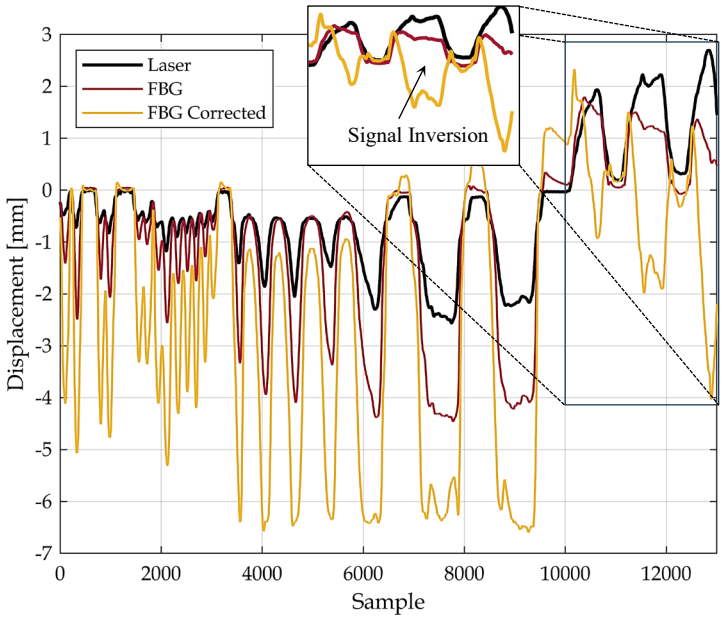

Figure 17 Reconstruction of the dynamic displacement using the down-selected neural network.

4.0 CONCLUSION

This paper has introduced the topics of shape sensing using fibre Bragg gratings for applications in hypersonic structures. A simple cantilever model is first studied which shows that a variety of models could potentially be used to reconstruct the displacement of a structure. Following this, a scramjet inlet ramp is studied as an applied case study. A finite element model of the ramp is constructed, from which surrogate data is produced to train and assess several neural networks. It was shown that there were errors between the predicted strains and those measured from the FBGs that contributed to the errors. Whilst the neural network suitably captured the trends and spectral response of the experimental model, displacements were under-predicted and over-predicted under static and dynamic loading, respectively. This result implies that a time dependent component should be included, and autoregressive neural networks should be explored. Shape sensing of hypersonic structures is of great importance and should be a continued area of research. Future work could aim to develop methods for the optimisation of sensor layouts, prediction of performance under aerothermoelastic loading (by coupling with a reduced order model), and the incorporation of temperature dependence.

ACKNOWLEDGMENTS

This research was supported by the Air Force Office of Scientific Research under award number FA2386-22-1-4081. Any opinion, finding, and conclusions or recommendations expressed in this material are those of the authors and do not necessarily reflect the views of the United States Air Force. Numerical resources were provided by the National Computational Infrastructure (NCI), under the UNSW HPC Resource Allocation Scheme and the National Computational Merit Allocation Scheme (NCMAS) under project code fd8.

REFERENCES

[1] L. POLLOCK AND G. WILD, "An initial review of hypersonic vehicle accidents," *arXiv preprint arXiv:2110.06438,* 2021, doi: https://doi.org/10.48550/arXiv.2110.06438.

[2] L. POLLOCK, J. MORAN, AND A. J. NEELY, "Effects of Aerothermal Shape Distortion on Hypersonic Vehicle Performance in Cruise," in *25th AIAA International Space Planes and Hypersonic Systems and Technologies Conference*, 2023, p. 3033, doi: https://doi.org/10.2514/6.2023-3033.

[3] Z. TUTEN, A. J. NEELY, B. R. CAPRA, K. M. TALLURU, AND L. P. MCQUELLIN, "Design and Bench Testing of a Radiatively Heated Model for Hypersonic Fluid-Thermal-Structural Interaction Experiments," in *AIAA AVIATION 2022 Forum*, 2022, p. 3796, doi: https://doi.org/10.2514/6.2022-3796.

[4] J. WAGNER, A. VALDIVIA, K. YUCEIL, N. CLEMENS, AND D. DOLLING, "An experimental investigation of supersonic inlet unstart," in *37th AIAA Fluid Dynamics Conference and Exhibit*, 2007, p. 4352, doi: https://doi.org/10.2514/6.2007-4352.

[5] S. BHATTRAI, L. P. MCQUELLIN, G. CURRAO, A. NEELY, AND D. R. BUTTSWORTH, "Experimental study of the aeroelastic response and performance of a hypersonic intake," in *23rd AIAA International Space Planes and Hypersonic Systems and Technologies Conference*, 2020, doi: https://doi.org/10.2514/1.B38348.

[6] M. GHERLONE, P. CERRACCHIO, AND M. MATTONE, "Shape sensing methods: Review and experimental comparison on a wing-shaped plate," *Progress in Aerospace Sciences,* vol. 99, pp. 14-26, 2018, doi: https://doi.org/10.1016/j.paerosci.2018.04.001.

[7] G. WILD, L. POLLOCK, A. K. ABDELWAHAB, AND J. MURRAY, "The Need for Aerospace Structural Health Monitoring: A review of aircraft fatigue accidents," *International Journal of Prognostics and Health Management,* vol. 12, no. 3, 2021, doi: https://doi.org/10.36001/ijphm.2021.v12i3.2368

[8] A. A. PHOENIX, J. R. MAXWELL, AND G. B. GOODWIN, "Morphing high-temperature surfaces for shapeable hypersonic waverider vehicles," in *Smart Materials, Adaptive Structures and Intelligent Systems*, 2017, vol. 58264: American Society of Mechanical Engineers, p. V002T03A012, doi: https://doi.org/10.1115/SMASIS2017-3766.

[9] W. L. Ko and W. L. Richards, "Method for real-time structure shape-sensing," 2009.

[10] S. SEFATI, C. GAO, I. IORDACHITA, R. H. TAYLOR, AND M. ARMAND, "Data-driven shape sensing of a surgical continuum manipulator using an uncalibrated fiber Bragg grating sensor," *IEEE sensors journal,* vol. 21, no. 3, pp. 3066-3076, 2020, doi: https://doi.org/10.1109/JSEN.2020.3028208.

[11] M. GHERLONE, P. CERRACCHIO, M. MATTONE, M. DI SCIUVA, AND A. TESSLER, "Shape sensing of 3D frame structures using an inverse finite element method," *International Journal of Solids and Structures,* vol. 49, no. 22, pp. 3100-3112, 2012, doi: https://doi.org/10.1016/j.ijsolstr.2012.06.009.

[12] W. L. KO, W. L. RICHARDS, AND V. T. TRAN, "Displacement theories for in-flight deformed shape predictions of aerospace structures," 2007.

[13] G. DING, S. YUE, S. ZHANG, AND W. SONG, "Strain-deformation reconstruction of CFRP laminates based on Ko displacement theory," *Nondestructive Testing and Evaluation,* vol. 36, no. 2, pp. 145-157, 2021, doi: https://doi.org/10.1080/10589759.2019.1707200.

[14] W. L. KO, W. L. RICHARDS, AND V. T. FLEISCHER, "Applications of Ko displacement theory to the deformed shape predictions of the doubly-tapered Ikhana Wing," 2009.

[15] H. M. CHAN, A. R. PARKER, A. PIAZZA, AND W. L. RICHARDS, "Fiber-optic sensing system: overview, development and deployment in flight at NASA," in *2015 IEEE Avionics and Vehicle Fiber-Optics and Photonics Conference (AVFOP)*, 2015: IEEE, pp. 71-73, doi: https://doi.org/10.1109/AVFOP.2015.7356646.

[16] H. YANG AND W. WU, "A review: Machine learning for strain sensor-integrated soft robots," *Frontiers in Electronic Materials,* vol. 2, p. 1000781, 2022, doi: https://doi.org/10.3389/femat.2022.1000781.

[17] T. L. T. LUN, K. WANG, J. D. HO, K.-H. LEE, K. Y. SZE, AND K.-W. KWOK, "Real-time surface shape sensing for soft and flexible structures using fiber Bragg gratings," *IEEE Robotics and Automation Letters,* vol. 4, no. 2, pp. 1454-1461, 2019, doi: https://doi.org/10.1109/LRA.2019.2893036.

[18] S. MANAVI ROODSARI *et al.*, "Shape Sensing of Optical Fiber Bragg Gratings Based on Deep Learning," *Machine Learning: Science and Technology,* 2023, doi: https://doi.org/10.1088/2632-2153/acda10.

[19] M. GHERLONE, P. CERRACCHIO, M. MATTONE, M. DI SCIUVA, AND A. TESSLER, "An inverse finite element method for beam shape sensing: theoretical framework and experimental validation," *Smart Materials and Structures,* vol. 23, no. 4, p. 045027, 2014, doi: https://doi.org/10.1088/0964-1726/23/4/045027.

[20] U. PAPA, S. RUSSO, A. LAMBOGLIA, G. DEL CORE, AND G. IANNUZZO, "Health structure monitoring for the design of an innovative UAS fixed wing through inverse finite element method (iFEM)," *Aerospace Science and Technology,* vol. 69, pp. 439-448, 2017, doi: https://doi.org/10.1016/j.ast.2017.07.005.

[21] C. QUACH, S. VAZQUEZ, A. TESSLER, J. MOORE, E. COOPER, AND J. SPANGLER, "Structural anomaly detection using fiber optic sensors and inverse finite element method," in *AIAA Guidance, Navigation, and Control Conference and Exhibit*, 2005, p. 6357, doi: https://doi.org/10.2514/6.2005-6357.

[22] D. OBOE, L. COLOMBO, C. SBARUFATTI, AND M. GIGLIO, "Shape sensing of a complex aeronautical structure with inverse finite element method," *Sensors,* vol. 21, no. 4, p. 1388, 2021, doi: https://doi.org/10.3390/s21041388.

[23] C.-G. PAK, "Wing shape sensing from measured strain," *AIAA Journal,* vol. 54, no. 3, pp. 1068-1077, 2016, doi: https://doi.org/10.2514/1.J053986.

[24] L. POLLOCK AND G. WILD, "Temporary Fiber Bragg Grating Sensors for Static and Dynamic Strain Measurements in Hypersonic Wind Tunnels," 2023, doi: https://doi.org/10.31224/2929

[25] V. MISHRA, M. LOHAR, AND A. AMPHAWAN, "Improvement in temperature sensitivity of FBG by coating of different materials," *Optik,* vol. 127, no. 2, pp. 825-828, 2016, doi: https://doi.org/10.1016/j.ijleo.2015.10.014.

[26] W. HU, H. CAI, M. YANG, X. TONG, C. ZHOU, AND W. CHEN, "Fe–C-coated fibre Bragg grating sensor for steel corrosion monitoring," *Corrosion Science,* vol. 53, no. 5, pp. 1933-1938, 2011, doi: https://doi.org/10.1016/j.corsci.2011.02.012.

[27] N. KAPLAN, J. JASENEK, J. ČERVEŇOVÁ, AND M. UŠÁKOVÁ, "Magnetic optical FBG sensors using optical frequency-domain reflectometry," *IEEE Transactions on Magnetics,* vol. 55, no. 1, pp. 1-4, 2018, doi: https://doi.org/10.1109/TMAG.2018.2873405.

[28] L. POLLOCK, H. KLEINE, A. NEELY, AND G. WILD, "Measuring fluid structure interaction in a cantilevered panel using optical fiber Bragg Gratings," in *AIAA AVIATION 2023 Forum*, 2023, p. 3605, doi: https://doi.org/10.2514/6.2023-3605.

[29] S. BHATTRAI, A. J. NEELY, G. CURRAO, AND L. P. MCQUELLIN, "Impact of aeroelasticity on hypersonic intake performance," *International Soc. of Airbreathing Engines Paper ISABE-2019-24059, Canberra, Australia,* 2019.